

Robust Vibration Control and Angular Velocity Estimation of a Single-Axis MEMS Gyroscope Using Perturbation Compensation

Mehran Hosseini-Pishrobat¹ • Jafar Keighobadi¹

Received: 6 June 2017 / Accepted: 2 February 2018 © Springer Science+Business Media B.V., part of Springer Nature 2018

Abstract

This paper discusses a perturbation compensation-based robust vibration controller for single-axis MEMS gyroscope applications. The purpose is to obtain a robust and stable operation mode of the gyroscope and improve its capability in estimating time-varying angular velocities. First, based on the force-balancing operation mode, an estimator is designed for real-time identification of input angular velocities. Next, to facilitate the angular velocity sensing, a control system is designed that comprises a nominal controller gathered with a perturbation compensator. In the perturbation compensation stage, a nonlinear extended state observer (NESO) is designed to estimate the perturbations due to parametric uncertainty, undesired couplings, Coriolis acceleration and mechanical-thermal noises. In the nominal control stage, by applying the internal model principle, an output regulator is developed. The outputs of both NESO and nominal regulator are combined to attain the robust vibration control of the gyroscope. The closed-loop stability and robustness are analytically proved through Lyapunov's direct method. To show the effectiveness of the proposed closed-loop operation mode, extensive numerical simulations are carried out by the experimental data of an inertial navigation system (INS).

Keywords MEMS gyroscope · Perturbation compensation · Extended state observer · Vibration control · Angular velocity estimation

1 Introduction

MEMS angular rate gyroscopes are used in diverse fields such as attitude determination, homing, bioengineering, robotics, and automotive safety systems [1–3]. Elimination of bearings and mechanical wear, batch fabrication under low cost, low power consumption and capability of integration with electronics on the same silicon chip, are prominent advantages of the MEMS gyroscopes over the conventional rotating wheel or fiber-optic gyroscopes [4]. At the core of a MEMS gyroscope, there is a proof mass that can oscillate along two orthogonal directions, known as the drive and sense axes [4]. In the open-loop operation mode, the proof mass is forced to vibrate along

the drive axis. When the sensor is exposed to an angular velocity, the Coriolis force proportionally transfers the vibration to the sense axis [4, 5]. Under frequency matching condition, assuming that the vibration modes are merely coupled by the Coriolis force, the input angular velocity is estimated by demodulating the steady-state response of the sense axis. Since the proof mass vibrates along two in-plane directions, the sensor is merely affected by the angular velocities about the normal axis to the plane of both drive and sense axes. Hence, this type of gyroscope is called single-axis gyroscope. Despite the above-mentioned advantages and potentials, the performance of a practical vibratory gyroscope may decrease by a variety of factors. The manufacturing process of a MEMS gyroscope involves multiple microfabrication stages. Therefore, owing to the accumulation of the errors contributed by each step, the final product suffers from structural and geometric defects [6]. Fabrication imperfections along with environmental variations results in the mismatch of the natural frequencies and unwanted mechanical couplings of the gyroscope axes, known as the quadrature error [4, 5]. These errors degrade the open-loop performance of the gyroscope and limit the maximum attainable sensitivity by the sensor.

Published online: 28 February 2018



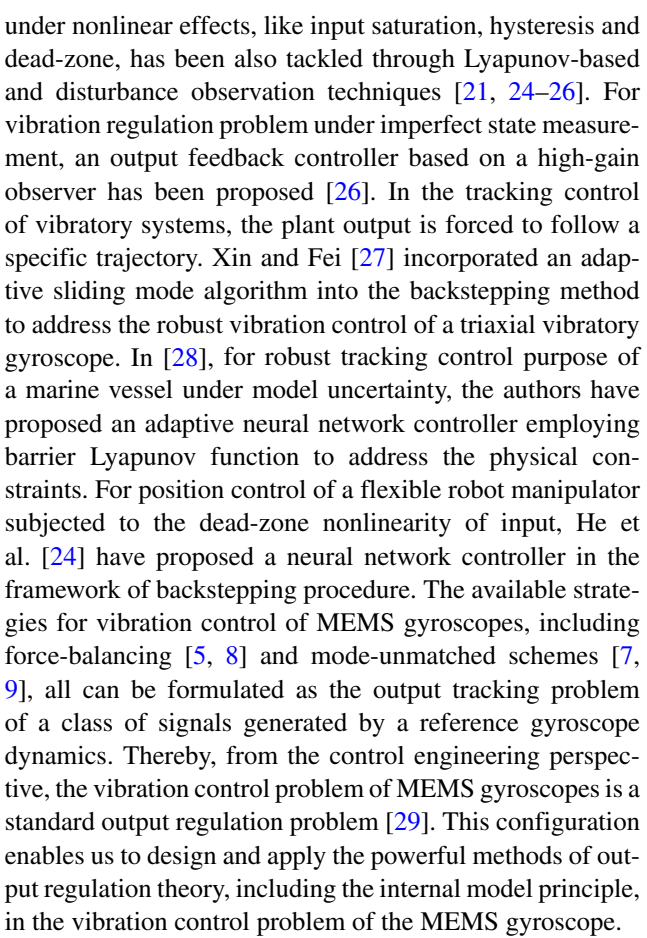
 [□] Jafar Keighobadi Keighobadi@tabrizu.ac.ir Mehran Hosseini-Pishrobat M.Hoseini92@ms.tabrizu.ac.ir

Faculty of Mechanical Engineering, University of Tabriz, P.C. 5166614766, Tabriz, Iran

High-performance demanding applications, like an inertial attitude determination system, require robust and stable operations of gyroscopes [1]. Therefore, a feedback control system is needed to enhance the stability and performance of the sensor. Various control methods, such as adaptive [5, 7], sliding mode [8] and adaptive sliding mode [9], have been proposed for MEMS gyroscopes. Combination of the sliding mode control with the artificial intelligence techniques has been reported as well [10]. To achieve optimal tracking control of the MEMS gyroscope in the presence of control constraints, the authors have proposed a model predictive control system in [11]. Active disturbance rejection control also has been applied to MEMS gyroscopes [12, 13].

Perturbation compensation controllers regulate the underlying system to the mathematical model based on which, a nominal control law is designed [14]. In this context, the perturbation refers to any discrepancy between the physical system and its nominal mathematical model, including parametric uncertainty, external disturbances, and noises [14]. Regarding the conventional control methods, the notable features of the perturbation compensation are as follows. (i) The approach departs from the classic robust and adaptive techniques that handle the perturbations passively and provides an active compensation framework for robustness. As a result, the method can deal with a vast class of uncertainties while covering a wide range of operating conditions [14, 15]. (ii) The main ingredients of a perturbation compensating feedback loop are a nominal controller and a perturbation compensator that robustifies the nominal system. This modular control structure allows shifting from a model-oriented design to a perturbation-oriented design by obviating the need for an accurate system model [16]. Extended state observers (ESOs) are powerful tools for estimating the state vector of a given system, as well as the perturbations affecting its dynamics. To improve the accuracy of the perturbation estimation, we propose a novel nonlinear extended state observer (NESO) for MEMS gyroscope applications by incorporating a suitable perturbation model. Such modification is advantageous considering that the perturbation signal of a MEMS gyroscope system carries information about the Coriolis force. Therefore, the estimated perturbation can be used for angular velocity estimation purposes.

The vibration control in mechanical and electromechanical systems, either as a regulation problem or as a tracking one, has been widely studied in recent years. In the regulation control aspect, vibration suppression of flexible structures is a conspicuous representative. In this regard, there are various vibration control methods in the literature such as differential flatness-based control [17], fuzzy logic-based control [18], Lyapunov-based boundary control [19, 20], disturbance observer-based adaptive control [21, 22] and iterative learning control [23]. Vibration suppression



The main contribution of this paper is to incorporate the methods of output regulation theory into the perturbation compensation control to realize a robust closed-loop MEMS gyroscope. Following a perturbation compensation control framework, we present the following novelties:

- 1. In the perturbation compensation aspect, we design a novel NESO to rectify the issues of the usual linear high-gain ESOs, including amplification of measurement noise, the peaking phenomenon, and inability to track time-varying perturbations [16, 30]. For accurate identification of the Coriolis force via perturbation estimation, we propose an internal model-based modified perturbation model. Moreover, the NESO applies a nonlinear gain function without resorting to the high-gain approach. As a result, the proposed NESO has a higher noise immunity compared to the conventional ESOs. A new framework is also developed for the NESO design based on absolute stability analysis of Lurie systems and linear matrix inequalities (LMIs).
- The internal model principle offers a robust solution for the output regulation problem by incorporating the internal model of the reference dynamics into the closed-loop system [29, 31]. Therefore, to improve



the structural robustness of the closed-loop system, particularly against perturbation compensation errors, we design an internal model-based vibration regulator as the nominal controller. We integrate this regulator with the NESO in the perturbation compensation coordination to control the MEMS gyroscope and identify the input angular velocity.

The rest of the paper is organized as follows. Dynamics of a vibratory gyroscope and basic modeling assumptions are explained in Section 2. Next, in Section 3 an angular velocity sensing algorithm is designed, and the associated control problem is formulated. Sections 4 and 5 elaborate the design and mathematical analysis of the perturbation compensator and the nominal regulator subsystems, respectively. Stability and robustness of the overall closed-loop system are investigated in Section 6. Software simulation by applying practical test data are presented in Section 7. Finally, the concluding remarks and future directions are given in Section 8.

Notation The notation used throughout the paper is quite standard. The Euclidean vector norm and the associated induced matrix norm are denoted by $\|.\|$. The truncated \mathcal{L}_2 norm of the signal $\chi: \mathbb{R}^+ \to \mathbb{R}^n$, over the interval [0,T], is defined as $\|\chi\|_{\mathcal{L}_{2T}} \triangleq \sqrt{\int_0^T \chi^\top(t)\chi(t)}\,\mathrm{d}t$. The zero and identity matrices of appropriate dimensions are denoted by I and O, respectively. The set of eigenvalues of a given matrix (.) is denoted by $\lambda(.)$. The operators $\lambda_{min}(.)$ and $\lambda_{max}(.)$ return the minimum and maximum eigenvalues of the Hermitian matrix (.), respectively. For a symmetric matrix $P \in \mathbb{R}^{n \times n}$ the notation $P \leq 0$ implies that P is negative semidefinite. The notation $\mathrm{col}(.,.,\ldots)$ stands for a vector obtained by stacking the argument vectors and, $\mathrm{diag}(.,.,\ldots)$ defines a diagonal matrix. The standard signum function is denoted by $\mathrm{sign}(.)$.

2 Mathematical Modeling of MEMS Gyroscope System

The mechanical model of a single-axis MEMS gyroscope, shown in Fig. 1, is approximated as a two-degrees-of-freedom (2-DOF) system comprising the proof mass, elastic elements, and damping components. The symbols used for the description of the gyroscope system are summarized in Table 1. The dynamics of the gyroscope should be considered with respect to the body-fixed frame, $\{xyz\}$. The mechanical configuration of the proof mass in the reference frame $\{xyz\}$ is specified by its displacements x and y along the respective axes with the constraint, z=0. As the typical operating condition of the sensor, the gyroscope frame $\{xyz\}$ is exposed to the angular velocity $\Omega_{z}(t)$, about

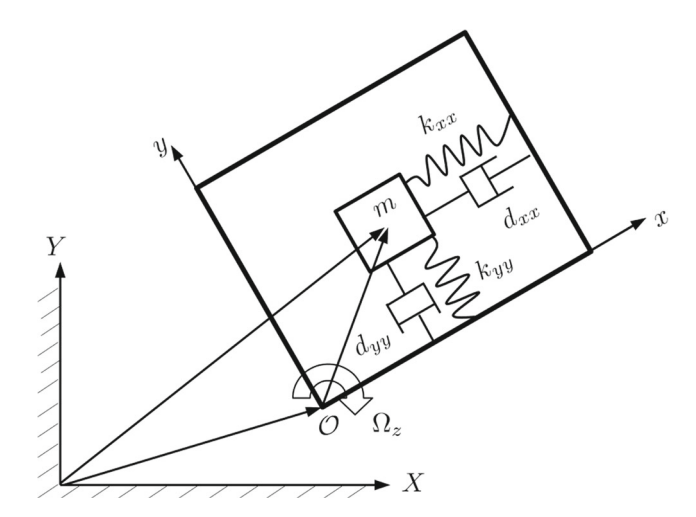


Fig. 1 Schematics of a single-axis MEMS gyroscope

the z axis, with respect to the inertial frame $\{XYZ\}$. The signal $\Omega_z \colon \mathbb{R}^+ \to \mathbb{R}$ is bounded over the time interval of the operation. In derivation of the gyroscope dynamics equations, the following practical assumptions are applied;

- The magnitude and the frequency ranges of the input angular velocities are much lower than the natural frequencies of the gyroscope. Hence, the associated second order terms and centripetal forces are negligible.
- 2. The acceleration of the point \mathcal{O} , with respect to the inertial frame, $\{XYZ\}$ is negligible.

By Newtonian formalism, the equations of motion of the gyroscope can be obtained by calculating the acceleration of the proof mass with respect to the inertial frame, $\{XYZ\}$ [4, 11]. Following this approach, we obtain

$$M\ddot{q} + D\dot{q} + Kq = u + 2\Lambda(t)\dot{q},\tag{1}$$

where $q \triangleq [x, y]^{\top} \in \mathbb{R}^2$ is the vector of generalized coordinates, $u \triangleq [u_x, u_y]^{\top} \in \mathbb{R}^2$ is the control input vector of electrostatic forces; $M \in \mathbb{R}^{2 \times 2}$, $D \in \mathbb{R}^{2 \times 2}$, $K \in \mathbb{R}^{2 \times 2}$ and $\Lambda : \mathbb{R}^+ \to \mathbb{R}^{2 \times 2}$ denote the inertia, damping, stiffness and Coriolis force matrices, respectively. The components of these matrices are determined as

$$\begin{split} M = & \begin{bmatrix} m & 0 \\ 0 & m \end{bmatrix}, \ D = \begin{bmatrix} d_{xx} & d_{xy} \\ d_{xy} & d_{yy} \end{bmatrix}, \ K = \begin{bmatrix} k_{xx} & k_{xy} \\ k_{xy} & k_{yy} \end{bmatrix}, \\ \Lambda(t) = & \begin{bmatrix} 0 & m\Omega_z(t) \\ -m\Omega_z(t) & 0 \end{bmatrix}. \end{split}$$

2.1 Basic Considerations

To obtain an appropriate mathematical model of the gyroscope, the following considerations are given for the system uncertainty and constraints;



Table 1 Symbols of the MEMS gyroscope system along with the numerical values

Symbol	Description	Value
$\{XYZ\}$	The inertial reference frame	N/A*
$\{xyz\}$	The body-fixed reference frame	N/A
\mathcal{O}	The origin of the $\{xyz\}$ frame	N/A
m	Proof mass	$5.095 \times 10^{-7} \text{ kg}$
k_{xx}	Linear stiffness constant along x axis	$349.7647 \pm 10\% \text{ N/m}$
k_{yy}	Linear stiffness constant along y axis	$525.2254 \pm 10\% \text{ N/m}$
k_{xy}	Coupling stiffness constant	17.4882 N/m
d_{xx}	Viscous damping constant along x axis	$1.335 \times 10^{-6} \pm 10\%$ N.s/m
d_{yy}	Viscous damping constant along y axis	$1.636 \times 10^{-6} \pm 10\%$ N.s/m
d_{xy}	Coupling damping constant	$6.7 \times 10^{-8} \text{ N.s/m}$
w_0	Reference frequency	10^3 Hz
q_0	Reference length	10^{-6} m

^{*} Not applicable

Consideration 1 Owing to imperfections of fabrication technologies and environmental variations, the parameters of the gyroscope model are approximately assigned. More explicitly,

$$d_{ij} = d_{ij}^{n} + \Delta d_{ij},$$

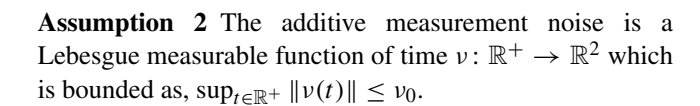
$$k_{ij} = k_{ij}^{n} + \Delta k_{ij}, i, j \in \{x, y\}.$$

The parameters with the superscript n stand for the known nominal values and the symbol, Δ represents the unknown variations with respect to the nominal parts. If a parameter is not known, the corresponding nominal value is set to zero. Moreover, the proof mass is assumed to be known precisely. Based on this argument, the damping and the stiffness matrices are decomposed into the respective nominal and unknown parts. That is, $D = D_n + \Delta D$ and $K = K_n + \Delta K$.

Consideration 2 Owing to the Brownian motion of the gas molecules surrounding the sensor, the mechanical-thermal noise affects the gyroscope dynamics as an input disturbance [32]. We model this disturbance by the following assumption.

Assumption 1 The mechanical-thermal noise is a Lebesgue measurable bounded signal $\tau\colon\mathbb{R}^+\to\mathbb{R}^2$ such that, $\sup_{t\in\mathbb{R}^+}\|\tau(t)\|\leq\tau_0$.

Consideration 3 The output vector of the gyroscope system is obtained by measuring the displacements of the proof mass along the x and y axes. The most widely used sensing mechanism in practice is of capacitive detection type, which offers advantages like ease of implementation, low power consumption, and low temperature sensitivity [4]. Furthermore, the measured signals are contaminated by electrical noise of the sensing interface circuit. We model this noise by the following assumption.



2.2 Nondimensionalization

Considering the diversified scales of the MEMS gyroscope parameters, the equations of motion (1) of the system are normalized. To this end, the following dimensionless variables are introduced;

$$\begin{split} &\frac{q}{q_0} \rightarrow q, \; \frac{u}{mq_0w_0^2} \rightarrow u, \; \frac{D}{mw_0} \rightarrow D, \; \frac{K}{mw_0^2} \rightarrow \\ &K, \; \frac{\Lambda(.)}{w_0} \rightarrow \Lambda(.), \; \; \frac{\tau}{mq_0w_0^2} \rightarrow \tau, \frac{v}{q_0} \rightarrow v. \end{split}$$

Based on the aforementioned formulation of the gyroscope system and Considerations 1-3, the gyroscope dynamics is rewritten as

$$\ddot{q} + D_n \dot{q} + K_n q = u + f(q, \dot{q}, t). \tag{2}$$

The parametric uncertainty and mechanical-thermal disturbance are lumped into the matched perturbation term $f: \mathbb{R}^2 \times \mathbb{R}^2 \times \mathbb{R}^+ \to \mathbb{R}^2$, given by

$$f(q, \dot{q}, t) = -\Delta Kq - (\Delta D - 2\Lambda(t))\dot{q} + \tau(t).$$

3 Angular Velocity Estimation and Statement of the Control Method

In the dynamics of a MEMS gyroscope, two fast and slow time-scales are defined by the oscillation frequency of the proof mass and the input angular velocity, respectively [6]. Hence, by isolating and proper filtering of lowfrequency components of the gyroscope dynamics, the



angular velocity can be estimated [12]. To this end, we formulate the control strategy in the force-balancing framework along with low-pass filtering-based angular velocity estimation. For a force-balanced gyroscope, the reference dynamics is conceived as a 1-DOF undamped oscillator along the *x*-axis. More specifically

$$\ddot{x}_m + w_1^2 x_m = 0, \ x_m(0) = 0, \ \dot{x}_m(0) = x_0 w_1, \tag{3}$$

where w_1 is the resonant frequency of the reference dynamics and x_0 is the desired amplitude. Along the y-axis, the motion of the proof mass is continuously detected and driven to zero:

$$y_m(t) = 0, \ \forall t \in \mathbb{R}^+. \tag{4}$$

Assuming that the controlled trajectory of the proof mass follows the reference signal, the *y*-component of the perturbation is

$$f_{y}(t) = -\Delta k_{xy} x_{0} \sin(w_{1}t) - (\Delta d_{xy} + 2\Omega_{z}(t)) x_{0} w_{1} \cos(w_{1}t) + \tau_{y}(t).$$

The quadrature and Coriolis forces have the relative phase shift of $\pi/2$. Thereby, multiplying both sides of (5) by $\cos^3(w_1t)$ and performing straightforward algebraic manipulations, we obtain the following relation for the low-frequency components of (5):

$$Q(-f_y(t)\cos^3(w_1t)) \approx \frac{3}{8}x_0w_1\left(\Delta d_{xy} + 2\Omega_z(t)\right),\tag{6}$$

where Q denotes a low-pass filtering operator. Assuming that an estimate $f_y^{est}(.)$ of $f_y(.)$ is available, we propose the following angular velocity estimator;

$$\hat{\Omega}_z(t) = \frac{4}{3x_0 w_1} Q(-f_y^{est}(t) \cos^3(w_1 t)) + \Omega_0.$$
 (7)

The constant, $\Omega_0 \in \mathbb{R}$ is a fixed bias term that accounts for the zero rate output (i.e., the output for $\Omega_z(t) \equiv 0$) of the sensor

Based on the concept of perturbation compensation, we propose a 2-DOF control system composed of the following parts:

- 1. Nominal control: According to the nominal gyroscope model, the nominal control input $u_n \in \mathbb{R}^2$ is designed to actively regulate the gyroscope vibration to the reference trajectory.
- 2. Perturbation compensation: The NESO is applied to continuously estimate and cancels out the perturbation, $f(q, \dot{q}, t)$.

In the proposed closed-loop mode of operation, the NESO facilitates functionality of the angular velocity estimator (7) as well as the perturbation compensation. The block diagram of the closed-loop system is illustrated in Fig. 2.

Remark 1 Theoretically, any frequency w_1 , which is large enough compared to the frequency span of the input angular velocities, can be used as the x-axis excitation frequency. From a practical point of view, operating in the resonance condition maximizes the amplification factor of the gyroscope. Therefore, matching the reference and natural frequencies significantly reduces magnitudes of the required steady-state excitation voltages [4, 11].

Remark 2 The perturbation estimation f_y^{est} in the right-hand side of (7) includes contributions of two separate parts, which are obtained through different channels. The first part, is directly available from the NESO of the perturbation compensator subsystem and the other, is computed according to the y-axis balancing control force because, $u_y + f_y \approx 0$ as $y, \dot{y}, \ddot{y} \rightarrow 0$. In fact, each one of these two parts gives an estimate of the perturbation f_y . We explain the optimal combination of these estimates in Section 7.3.

4 Perturbation Compensator Design

In conventional ESOs, linear high-gain differentiators are used to estimate the perturbation, conceived as an additional state variable [15]. These ESOs, however, cannot reconstruct fast time-varying perturbation signals [16]. The lack stems from modeling the perturbation as an extra integrator added to the system. Consequently, the estimation error converges to zero merely for step-type perturbations. As argued by Madonski and Herman [16], to improve the perturbation estimation convergence, more effective models are required to capture the basic characteristics of the perturbation. In this regard, we model the perturbation signal $f(t) \triangleq f(q(t), \dot{q}(t), t)$ as follows;

$$f(t) = \zeta(t) + C_f \omega(t), \tag{8}$$

where $\zeta(.)$ is a differentiable signal, C_f is a real matrix of proper dimension and $\omega(.) \in \mathbb{R}^p$ is the solution of the following autonomous system;

$$\dot{\omega} = S\omega. \tag{9}$$

The perturbation $f(q, \dot{q}, t)$ depends linearly on the gyroscope state variables. Thereby, an appropriate perturbation model can be obtained by setting the system (9) as the internal model of the reference vibration trajectory. We will expand on this subject in Section 5. But, without loss of generality, the following assumptions are made;

- 1. The pair (C_f, S) is observable.
- 2. All eigenvalues of the matrix *S* lie on the imaginary axis with multiplicity one in the minimal polynomial; this



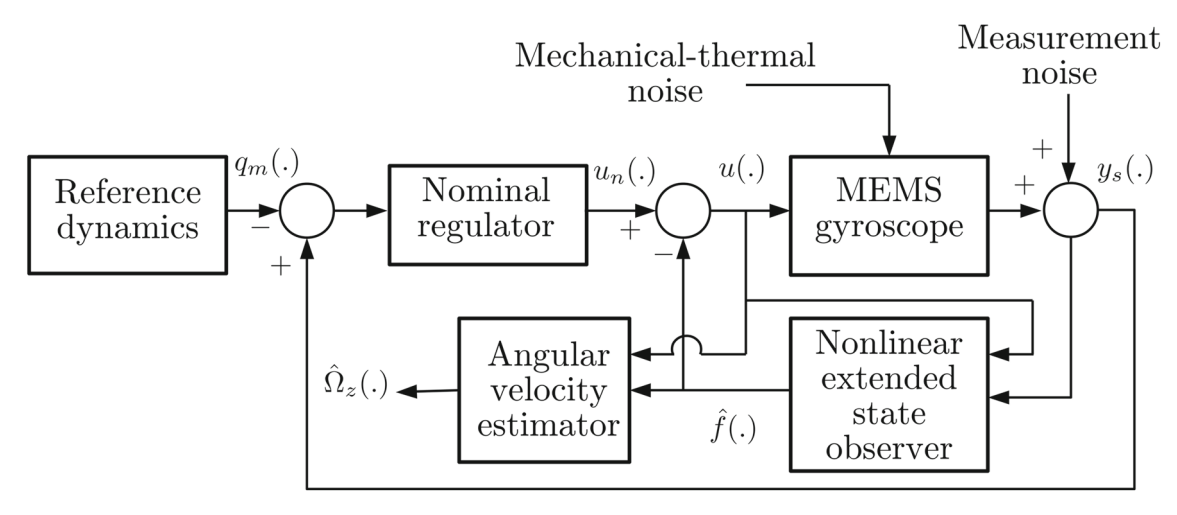


Fig. 2 Block diagram of the proposed closed-loop system

assumption ensures persistence and boundedness of the perturbation signal [29].

We use the state variables $x_1 = q$, $x_2 = \dot{q}$ and $x_3 = \zeta$ to transform the dynamic model of the gyroscope (2) into the following extended state-space system;

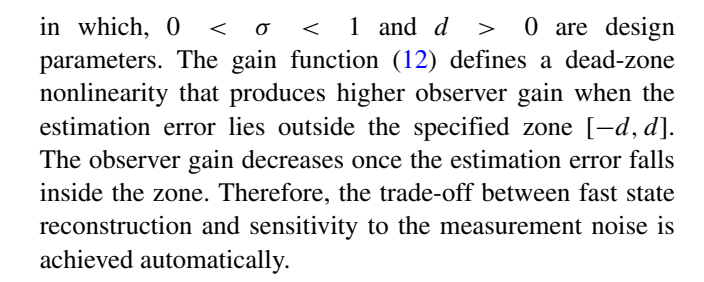
$$\dot{x}_{1} = x_{2},
\dot{x}_{2} = -K_{n}x_{1} - D_{n}x_{2} + x_{3} + C_{f}\omega + u,
\dot{x}_{3} = h(t),
\dot{\omega} = S\omega,
y_{s} = x_{1} + \nu(t),$$
(10)

where $h(t) \triangleq \mathrm{d}\zeta(t)/\mathrm{d}t$ and y_s denotes the measurement vector contaminated by the noise v(.). The physical construction and the working conditions of the gyroscope constrain the signal h(.) to be bounded as $\sup_{t \in \mathbb{R}} \|h(t)\| \le h_0$ [13]. To reconstruct the perturbation signal, the following NESO is used;

$$\dot{\hat{x}}_{1} = \hat{x}_{2} + H_{1}g(y_{s} - \hat{x}_{1}),
\dot{\hat{x}}_{2} = -K_{n}\hat{x}_{1} - D_{n}\hat{x}_{2} + \hat{x}_{3} + C_{f}\hat{\omega} + u + H_{2}g(y_{s} - \hat{x}_{1}),
\dot{\hat{x}}_{3} = H_{3}g(y_{s} - \hat{x}_{1}),
\dot{\hat{\omega}} = S\hat{\omega} + H_{4}g(y_{s} - \hat{x}_{1}),$$
(11)

where \hat{x}_i and $\hat{\omega}$, respectively, are the estimates of x_i and ω , H_i are design matrices of compatible dimensions and $g \colon \mathbb{R}^2 \to \mathbb{R}^2$ is a locally Lipschitz nonlinear vector function satisfying $g(z) = [g_1(z_1), g_2(z_2)]^{\top}$ and g(0) = 0. The function g(.) defines the observer innovation process, and its structure determines the convergence and noise robustness properties of the observer. Based on the nonlinear observer of Prasov and Khalil [30], we propose the gain function

$$g_i(z_i) = \begin{cases} \sigma z_i, & |z_i| \le d \\ z_i + d(\sigma - 1)\operatorname{sign}(z_i), & |z_i| > d \end{cases}, \tag{12}$$



Remark 3 According to the NESO (11), the estimated perturbation is obtained as $\hat{f}(t) = \hat{x}_3(t) + C_f \hat{\omega}(t)$.

4.1 Convergence Analysis

In order to investigate convergence of the NESO (11), we introduce the following error variables;

$$\eta_i \triangleq x_i - \hat{x}_i, \ i = 1, 2, 3,
\eta_4 \triangleq \omega - \hat{\omega}.$$

Setting $\eta \triangleq \operatorname{col}(\eta_1, \eta_2, \eta_3, \eta_4)$ and $\xi \triangleq \eta_1$, we obtain the following differential equation for the estimation error;

$$\dot{\eta} = A_0 \eta + Hg(\xi + \nu(t)) + Qh(t),
\xi = C_0 \eta,$$
(13)

where

$$A_{0} = \begin{bmatrix} O & I & O & O \\ -K_{n} & -D_{n} & I & C_{f} \\ O & O & O & O \\ O & O & O & S \end{bmatrix}, \ H = \begin{bmatrix} -H_{1} \\ -H_{2} \\ -H_{3} \\ -H_{4} \end{bmatrix},$$

$$Q = \begin{bmatrix} O \\ O \\ I \\ O \end{bmatrix}, \ C_{0} = \begin{bmatrix} I & O & O & O \end{bmatrix}.$$



Remark 4 According to the definition (12), the nonlinear gain function g(.) has two particularly important features;

1. It admits global Lipschitz continuity;

$$\|g(\xi_2) - g(\xi_1)\| \le \|\xi_2 - \xi_1\|, \ \forall \xi_1, \xi_2 \in \mathbb{R}^2.$$
 (14)

2. It is a sector-bounded nonlinearity in the following sense [33, 34];

$$\sigma \xi^{\mathsf{T}} \xi \le \xi^{\mathsf{T}} g(\xi) \le \xi^{\mathsf{T}} \xi, \ \forall \xi \in \mathbb{R}^2.$$
 (15)

The following assumption forms the basis for establishing the convergence of the NESO.

Assumption 3 The nominal NESO error dynamics defined as

$$\dot{\eta} = A_0 \eta + Hg(\xi),
\xi = C_0 \eta,$$
(16)

has a globally exponentially stable equilibrium at the origin.

Theorem 1 Under Assumptions 1-3, the solutions of the error system (13) are globally bounded and after a finite transient time T_0 , the following bound is valid for an arbitrary small $\rho_0 > 0$ and some constants $\mu_0 \ge 0$ and $\mu_1 \ge 0$;

$$\|\eta(t)\| \le \rho_0 + \mu_0 \nu_0 + \mu_1 h_0. \tag{17}$$

Proof The error dynamics (13) is rewritten in the following form:

$$\dot{\eta} = A_0 \eta + Hg(\xi) + H(g(\xi + \nu(t)) - g(\xi)) + Qh(t),$$

 $\xi = C_0 \eta.$

(18)

By Assumption 3, there exists a Lyapunov function $V(\eta)$ whose time derivative along the trajectories of (16) satisfies (see, [34]);

$$\frac{\frac{\mathrm{d}V(\eta)}{\mathrm{d}t}}{\frac{\mathrm{d}t}{\partial\eta}}|_{(16)} \leq -\beta_0 V(\eta),
\|\frac{\frac{\partial V(\eta)}{\partial\eta}}{\frac{\partial\eta}{\partial\eta}}\| \leq \beta_1 \sqrt{V(\eta)},
\|\eta\| \leq \beta_2 \sqrt{V(\eta)},$$
(19)

where β_0 , β_1 , $\beta_2 > 0$. Differentiating $V(\eta)$ with respect to time along the solutions of (18) and using the property of Lipschitz continuity (18), we obtain the following inequality;

$$\frac{dV(\eta)}{dt} \mid_{(18)} \le -\beta_0 V(\eta) + (\beta_3 v_0 + \beta_4 h_0) \sqrt{V(\eta)}, \quad (20)$$

with $\beta_3 = \beta_1 ||H||$ and $\beta_4 = \beta_1 ||Q||$. Dividing both sides of (20) by $2\sqrt{V(\eta)}$ and invoking the comparison lemma of differential inequalities [34], we get:

$$\sqrt{V(\eta(t))} \le \exp(-\frac{\beta_0 t}{2})\sqrt{V(\eta(0))} + \frac{\beta_3 v_0 + \beta_4 h_0}{\beta_0} \left(1 - \exp(-\frac{\beta_0 t}{2})\right). \tag{21}$$

Thereby

$$\|\eta(t)\| \le \beta_2 \exp(-\frac{\beta_0 t}{2}) \sqrt{V(0)} + \beta_2 \frac{\beta_3 \nu_0 + \beta_4 h_0}{\beta_0} \left(1 - \exp(-\frac{\beta_0 t}{2})\right).$$
 (22)

Considering nonzero exponentially decaying term, after the time T_0 given by

$$T_0 \triangleq \frac{2}{\beta_0} \log \left(\frac{\mid \beta_2 \sqrt{V(\eta(0))} - (\beta_2/\beta_1)(\beta_3 \nu_0 + \beta_4 h_0) \mid}{\rho_0} \right),$$

the ultimate bounded (17) holds with $\mu_0 \triangleq \beta_2 \beta_3 / \beta_0$ and $\mu_1 \triangleq \beta_2 \beta_4 / \beta_0$. In the special case of zero exponential term that the initial condition of the system satisfies

$$V(\eta(0)) = \left(\frac{\beta_2}{\beta_1}(\beta_3\nu_0 + \beta_4 h_0)\right)^2,$$

the transient phase vanishes and $T_0 = 0$.

4.2 Design of the NESO via LMIs

The key assumption of Theorem 1 is the exponential stability of the equilibrium solution of the nominal error dynamics (16). This assumption entails the existence of a Lyapunov function that decreases exponentially along the system trajectories (see the proof of Theorem 1 for more details). Here, we propose a numerical scheme to construct such a Lyapunov function and to design the gain matrices H_i . To this end, the exponential stability of (16) is formulated as the quadratic stabilization of a standard Lurie system [33, 34]. To further improve the convergence behavior of the NESO, we employ regional pole placement for the linearized nominal error system. Accordingly, the eigenvalues of the Jacobian matrix $A_0 + \sigma HC_0$ are confined to the following strip in the complex plane for given constants a > 0 and b > a;

$$\mathcal{D}_s \triangleq \{ s \in \mathbb{C} \mid -b \le \Re(s) \le -a \}. \tag{23}$$

Theorem 2 For given positive constants a, b and β_0 , assume there exist a positive definite matrix P, a matrix Y and a positive scalar γ satisfying

$$\begin{bmatrix} PA_0 + A_0^\top P + \beta_0 P - \gamma \sigma C_0^\top C_0 & Y + \gamma \left(\frac{1+\sigma}{2}\right) C_0^\top \\ Y^\top + \gamma \left(\frac{1+\sigma}{2}\right) C_0 & -\gamma I \end{bmatrix} \le 0, (24a)$$

$$PA_0 + A_0^{\top} P + \sigma Y C_0 + \sigma C_0^{\top} Y^{\top} + 2aP \le 0,$$
 (24b)

$$-PA_0 - A_0^{\top} P - \sigma Y C_0 - \sigma C_0^{\top} Y^{\top} - 2bP \le 0.$$
 (24c)

Then,

- 1. The gain matrix $H = P^{-1}Y$ in conjunction with the Lyapunov function $V(\eta) = \eta^{\top} P \eta$ guarantees the exponential stability of the nominal error system (16).
- 2. All eigenvalues of the matrix $A_0 + \sigma HC_0$ are in the region \mathcal{D}_s .



Proof Taking a positive constant β_0 , we seek a positive definite quadratic function $V(\eta) = \eta^{\top} P \eta$ that satisfies

$$\frac{\mathrm{d}V(\eta)}{\mathrm{d}t} \le -\beta_0 V(\eta). \tag{25}$$

It follows from (25) that

$$\eta^{\top} (PA_0 + A_0^{\top} P + \beta_0 P) \eta + 2\eta^{\top} P H g(\xi) \le 0,$$

which is equivalent to the following LMI;

$$\begin{bmatrix} PA_0 + A_0^\top P + \beta_0 P & PH \\ H^\top P & O \end{bmatrix} \le 0.$$
 (26)

The sector condition (15) is rephrased as the following LMI [33];

$$\begin{bmatrix} \sigma C_0^{\top} C_0 & -\left(\frac{1+\sigma}{2}\right) C_0^{\top} \\ -\left(\frac{1+\sigma}{2}\right) C_0 & I \end{bmatrix} \le 0.$$
 (27)

A sufficient condition for the exponential stability is the existence of a positive definite matrix P satisfying (26) whenever (27) holds. By the S-procedure [33], this statement equivalent to the existence of a positive γ for which, the LMI (24a) with $Y \triangleq PH$ is feasible. To prove the next result, first we note that all the eigenvalues of the matrix $A_0 + \sigma HC_0$ are in \mathcal{D}_s if and only if:

$$\Re \left(\lambda_i (A_0 + \sigma H C_0 + aI) \right) \le 0$$

$$\Re \left(\lambda_i (-A_0 - \sigma H C_0 - bI) \right) \le 0.$$

$$(28)$$

By Lyapunov's theorem on stability of linear system [33, 34], (28) is equivalent to the existence of a positive definite matrix P satisfying (24b) and (24c).

5 Nominal Controller Design

As discussed in Section 3 for the force-balancing mode of operation, the equations of motion of the reference gyroscope system are;

$$\begin{cases} \ddot{x}_m + w_1^2 x_m = 0, \\ y_m(t) = 0, \ \forall t \in \mathbb{R}^+. \end{cases}$$
 (29)

Considering $q_m \triangleq [x_m, y_m]^{\top}$, the goal of the nominal controller is to drive the tracking error

$$e \triangleq q - q_m \tag{30}$$

to zero, while guaranteeing boundedness of the all other signals. Considering a steady-state condition in which, the nominal and the reference dynamics coincide with each other, we obtain

$$\begin{aligned}
\bar{q} &= q_m, \\
\dot{\bar{q}} &= \dot{q}_m, \\
\bar{u}_n &= \ddot{q}_m + D_n \dot{q}_m + K_n q_m.
\end{aligned} \tag{31}$$

The vector $\bar{q} \in \mathbb{R}^2$ denotes the steady-state generalized coordinates, and $\bar{u}_n \in \mathbb{R}^2$ is the corresponding control

input, which supplies the required energy to match the nominal and the reference dynamics. The equations in (31) are known as the regulator equations in the output regulation literature, and their solvability is instrumental in designing the output regulator [29, 31]. We observe from (31) that the regulator equations of a vibratory gyroscope admit a unique solution $(\bar{q}(.), \bar{u}_n(.))$ for a given reference trajectory $q_m(.)$. We define a composite system that gathers both nominal and reference dynamics;

$$\Sigma_c : \begin{cases} \ddot{q} + D_n \dot{q} + K_n q = u_n, \\ \ddot{x}_m + w_1^2 x_m = 0, \\ y_m(t) = 0. \end{cases}$$
(32)

From a geometrical point of view, the regulator equations (31) define a *controlled invariant subspace* of Σ_c given by [29, 31];

$$\mathcal{M} \triangleq \{(q, \dot{q}, q_m, \dot{q}_m) \in \mathbb{R}^8 \mid q - q_m = 0, \dot{q} - \dot{q}_m = 0\}.$$
 (33)

If the initial conditions of Σ_c lie on \mathcal{M} , with the control input \bar{u}_n , the trajectories of the system will evolve on \mathcal{M} for all times $t \in \mathbb{R}^+$ and the tracking error (30) will be identically equal to zero. Accordingly, to solve the output regulation problem globally, the subspace \mathcal{M} should be rendered attractive so that all of the system trajectories converge to those defined by the regulator equations (31). To do this, we need to define an appropriate distance coordinate measuring the attractivity of \mathcal{M} , and then, drive this coordinate to zero. The simplest distance coordinate-immediately defined from the regulator equations (31)-is $\delta q \triangleq q - \bar{q}$ with the associated control variable $\delta u_n \triangleq u_n - \bar{u}_n$. This leads to the so-called feedforward design widely used in the reported MEMS gyroscope control systems. However, due to the direct dependence of the distance coordinate to the solution of the regulator equations, the approach lacks robustness against perturbations (see [31] for more details). To perform a more robust design, we adopt a different method based on the internal model principle [29, 31]. Toward this end, we consider the characteristic polynomial associated with the reference dynamics (29);

$$\Gamma(s) \triangleq s^2 + w_1^2,\tag{34}$$

where $s \triangleq d/dt$ is the time differentiation operator. Accordingly, we define the following auxiliary variables;

$$q_d(t) \triangleq \Gamma(s)q(t),$$

 $u_d(t) \triangleq \Gamma(s)u_n(t).$

Proposition 1 The variable $q_d(.)$ in conjunction with $u_d(.)$ defines a distance coordinate in the sense that both $q_d(.)$ and $u_d(.)$ are equivalent to zero, if and only if $\operatorname{col}(q, \dot{q}, q_m, \dot{q}_m) \in \mathcal{M}$ and $u_n \equiv \bar{u}_n$.



Proof It directly follows from the definition of $\Gamma(s)$ that

$$\Gamma(s)q_m(t) = 0, \ \Gamma(s)\bar{u}_n(t) = 0, \ \forall t \in \mathbb{R}^+.$$

Hence, when the trajectories of the gyroscope lie on \mathcal{M} , both $q_d(.)$ and $u_d(.)$ are equal to zero for all times. Now, assuming that $q_d(.)$ and $u_d(.)$ are equivalent to zero for all times, the following differential equation holds;

$$\Gamma(s)q(t) = \Gamma(s)q_m(t), \ \forall t \in \mathbb{R}^+.$$

According to the regulator equations (31), we can always set the initial condition of the reference dynamics such that $q(0) = q_m(0)$ and $\dot{q}(0) = \dot{q}_m(0)$. Owing to the uniqueness theorem of solutions of linear differential equations [34], it follows that

$$q(t) = q_m(t), \ \forall t \in \mathbb{R}^+,$$

which also implies $u_n \equiv \bar{u}_n$ and hence, the trajectories belong to \mathcal{M} .

The variable $q_d(.)$ is conceived as a dynamic measure of the distance of the gyroscope system trajectories from the subspace \mathcal{M} , which incorporates the internal model of the reference dynamics. Using $\Gamma(s)$ as a differential operator, dynamics of $q_d(.)$ is obtained as

$$\ddot{q}_d + D_n \dot{q}_d + K_n q_d = u_d. \tag{35}$$

This equation cannot be used for regulation purposes since $q_d(.)$ is not measured. To overcome this issue, we apply the operator $\Gamma(s)$ to the tracking error (30):

$$\Gamma(s)e = q_d. \tag{36}$$

This differential equation describes the dynamic relation between the tracking error and the distance coordinate. Setting $X_{aug} \triangleq \operatorname{col}(q_d, \dot{q}_d, e, \dot{e}) \in \mathbb{R}^8$ both (35) and (36) are represented by the following augmented state-space equation;

$$\dot{X}_{aug} = A_{aug} X_{aug} + B_{aug} u_d,
e = C_{aug} X_{aug}.$$
(37)

The system matrices are

$$A_{aug} = \begin{bmatrix} O & I & O & O \\ -K_n & -D_n & O & O \\ O & O & I & O \\ I & O & -w_1^2 I & O \end{bmatrix}, \ B_{aug} = \begin{bmatrix} O \\ I \\ O \\ O \end{bmatrix},$$

$$C_{aug} = \begin{bmatrix} O & O & I & O \end{bmatrix}.$$

Regulation of the distance coordinate to zero is now converted to stabilization of the augmented system (37). To this end, we use the following dynamic output feedback controller:

$$\dot{X}_c = A_{aug}X_c + B_{aug}u_d + G(e - C_{aug}X_c),
 u_d = -FX_c,$$
(38)

where $X_c \in \mathbb{R}^8$ is the internal state of the controller and G and F are gain matrices of appropriate dimensions. The

matrices G and F can be designed using the standard linear control methods, such as eigenvalue assignment or linear quadratic regulator (LQR), to obtain an exponentially stable nominal closed-loop system. The distance coordinate q_d does not depend directly on the regulator equations (31) and therefore, perturbations of the nominal dynamics do not affect the proposed regulation scheme directly. From this perspective, applying the internal model of the reference dynamics is a robust approach to recover the solutions of the regulator equations [31].

Remark 5 The proposed regulation method uses the auxiliary control variable $u_d(.)$ in its feedback loop. The primary control signal $u_n(.)$ is obtained by applying the inverse filter of $\Gamma(s)$ to $u_d(.)$. That is, $u_n(t) = \Gamma^{-1}(s)u_d(t)$.

6 Closed-Loop Stability

According to the 2-DOF configuration of the proposed control system, the overall control input consists of two portions (see Fig. 2);

$$u(t) = u_n(t) - \hat{f}(t), \tag{39}$$

where $\hat{f}(.)$ denotes the estimated perturbation obtained from the NESO (11). The stability and convergence of the NESO (11) are established by the analysis results of Theorem 1 and design methods of Theorem 2. Hence, we focus on the effects of the perturbation compensation loop on the performance of the nominal regulator. On this basis, the equation of motion of the gyroscope becomes

$$\ddot{q} + D_n \dot{q} + K_n q = u_n + \tilde{f}(t), \tag{40}$$

where $\tilde{f}(t) \triangleq f(t) - \hat{f}(t)$ is the perturbation estimation error. We note that the main step in the regulation of the gyroscope output is the stabilization of the subspace \mathcal{M} , on the basis of the internal model principle. It is conceivable that the controlled trajectories of the gyroscope will converge to a small bounded neighborhood of the target subspace. To put the statement in a formal mathematical setting, we consider the nominal control system in conjunction with the perturbation compensator:

$$\dot{X}_{aug} = A_{aug} X_{aug} + B_{aug} (u_d + \psi(t)),$$

$$\dot{X}_c = A_{aug} X_c + B_{aug} u_d + G(e + v(t) - C_{aug} X_c),$$

$$u_d = -F X_c,$$
(41)

in which, $\psi(t) \triangleq \Gamma(s)\tilde{f}(t)$ is considered to be bounded as $\sup_{t \in \mathbb{R}^+} \|\psi(t)\| \leq \psi_0$. Using the aggregated state vector, $X \triangleq \operatorname{col}(X_{aug}, X_c)$ the closed-loop dynamics is described by the following state-space equation:

$$\dot{X} = A_{cl}X + B_{\psi}\psi(t) + B_{\nu}\nu(t), \tag{42}$$

where

$$\begin{split} A_{cl} &= \begin{bmatrix} A_{aug} & -B_{aug}F \\ GC_{aug} & A_{aug} - B_{aug}F - GC_{aug} \end{bmatrix}, \\ B_{\psi} &= \begin{bmatrix} B_{aug} \\ O \end{bmatrix}, \ B_{v} &= \begin{bmatrix} O \\ G \end{bmatrix}. \end{split}$$

Assumption 4 The gains G and F are designed such that A_{cl} is a Hurwitz stable matrix.

Remark 6 The pair (A_{aug}, B_{aug}) is controllable and (C_{aug}, A_{aug}) is observable. Thereby, there always exist gain matrices G and F that satisfy Assumption 4.

Theorem 3 Suppose that the NESO (11) is designed according to Theorem 2. Under Assumption 4, the trajectories of the system (42) are globally bounded and ultimately bounded. More specifically, after a finite transient time T_1 the following ultimate bound holds for some positives μ_2 , μ_3 and an arbitrary small positive ρ_1 ;

$$||X(t)|| \le \rho_1 + \mu_2 \psi_0 + \mu_3 \nu_0,\tag{43}$$

Proof Owing to Assumption 4, the matrix Lyapunov equation

$$P_{cl}A_{cl} + A_{cl}^{\top}P_{cl} = -2I,$$

admits a unique positive definite solution for P_{cl} . We consider the associated positive definite function, $\mathcal{V}(X) = X^{\top} P_{cl} X$. Direct calculations show that the time derivative of $\mathcal{V}(X)$, along the solutions of (42), satisfies the inequality

$$\frac{\mathrm{d}\mathcal{V}(X)}{\mathrm{d}t} \leq -\frac{2}{\lambda_{max}(P_{cl})}\mathcal{V}(X) + 2(\|P_{cl}B_{\psi}\|\psi_0 + \|P_{cl}B_{\nu}\|\nu_0)\sqrt{\frac{\mathcal{V}(X)}{\lambda_{min}(P_{cl})}}.$$

Using the similar procedure used in the proof of Theorem 1, it follows that

$$||X(t)|| \le \exp\left(\frac{-t}{\lambda_{max}(P_{cl})}\right) \sqrt{\frac{\mathcal{V}(0)}{\lambda_{min}(P_{cl})}} + \left(||P_{cl}B_{\psi}||\psi_{0} + ||P_{cl}B_{v}||\nu_{0}\right) \frac{\lambda_{max}(P_{cl})}{\lambda_{min}(P_{cl})} \left(1 - \exp\left(\frac{-t}{\lambda_{max}(P_{cl})}\right)\right).$$
(44)

Therefore, after the time T_1 given by

$$T_1 \triangleq \lambda_{max}(P_{cl}) \log \left(\left| \frac{1}{\rho_1} \sqrt{\frac{\mathcal{V}(0)}{\lambda_{min}(P_{cl})}} - \frac{\lambda_{max}(P_{cl})}{\rho_1 \lambda_{min}(P_{cl})} \left(\|P_{cl}B_{\psi}\| \psi_0 + \|P_{cl}B_{v}\| v_0 \right) \right| \right),$$

the ultimate bound (43) is valid with the following constants;

$$\mu_2 = \frac{\lambda_{max}(P_{cl})}{\lambda_{min}(P_{cl})} \|P_{cl}B_{\psi}\|, \ \mu_3 = \frac{\lambda_{max}(P_{cl})}{\lambda_{min}(P_{cl})} \|P_{cl}B_{\nu}\|.$$

The special case where

$$\mathcal{V}(X(0)) = \frac{\lambda_{max}^{2}(P_{cl})}{\lambda_{min}(P_{cl})} \left(\|P_{cl}B_{\psi}\|\psi_{0} + \|P_{cl}B_{\nu}\|\nu_{0} \right)^{2},$$



corresponds to no exponentially decaying transient phase, that is $T_1 = 0$.

7 Simulation Results

Numerical simulations are carried out using practical test data in MATLAB/ Simulink environment to verify the effectiveness of the proposed controller along with the angular velocity estimation algorithm. The gyroscope parameters and the reference values used for nondimensionalization are given in Table 1. The key parameters are taken from the dynamic model of the MIT-SOI MEMS gyroscope [7]. To resemble a real-time MEMS gyroscope application, four different angular velocity waveforms, taken from the vehicular test data of an inertial navigation system aided by GPS [35], are considered as the gyroscope inputs (see Fig. 3). The test was conducted using ADIS16407 inertial measurement unit (IMU) in which, the data of MEMS-grade gyroscopes were collected in a 50 Hz sampling rate [35]. The raw data sets are low-pass filtered to eliminate the high-frequency noises and obtain smooth angular velocity waveforms. At the initial time t = 0, the proof mass is assumed stationary in its unforced position. The perturbation model (8) is defined by the following observable pair $(C_f, S);$

$$S = \begin{bmatrix} O & I \\ -w_1^2 I & O \end{bmatrix}, \ C_f = \begin{bmatrix} I & O \end{bmatrix}.$$

In order to verify the tracking performance of the controller in various operating conditions, four different reference trajectories are considered:

Case I: $x_0 = 0.3 \ \mu \text{m}, w_1 = 5w_0 \text{ rad/s};$

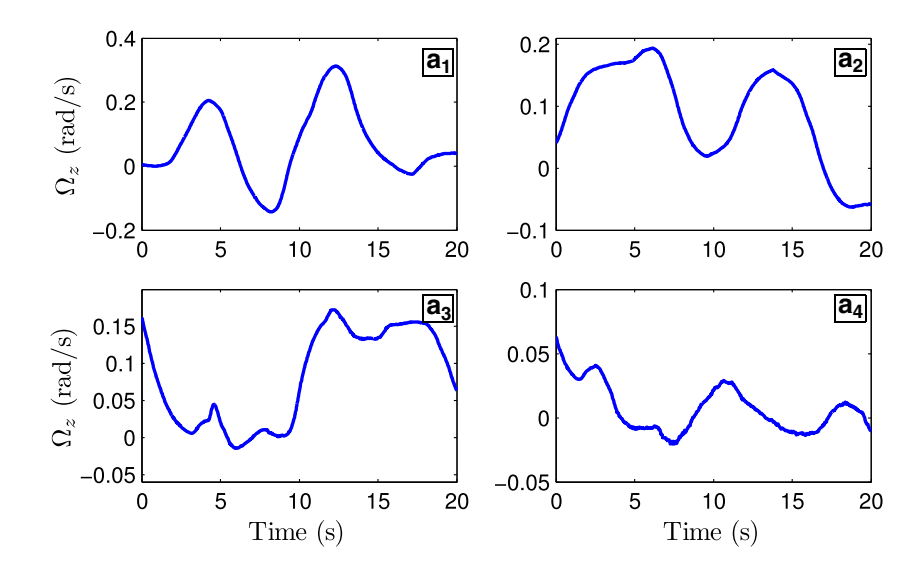
Case II: $x_0 = 0.8 \ \mu\text{m}, w_1 = 15w_0 \text{ rad/s};$

Case III: $x_0 = 0.5 \mu \text{m}, w_1 = 26.21 w_0 \text{ rad/s};$

Case IV: $x_0 = 0.7 \ \mu \text{m}, w_1 = 40 w_0 \text{ rad/s}.$

We note that the frequency of Case III coincides with the x-axis nominal natural frequency that, according to Remark 1, is more suitable for practical gyroscopes. The nonlinear gain function (12) is characterized by the parameters $\sigma=0.5$ and d=0.01. The gain matrices H_i of the observer (11) are designed using the results of Theorem 2. To this end, taking a=11, b=25 and $\beta_0=15$ the LMIs (24a)-(24c) are solved using CVX, which is a specialized package for solving convex programs [36, 37]. The results, summarized in Table 2, show that the exponential convergence of the nominal error system (16) along with the regional eigenvalue assignment are guaranteed. Using LQR, we design the controller (38) in such a way that the spectrum of the matrices $A_{aug} - B_{aug}F$ and $A_{aug} - GC_{aug}$ lie on the left of the lines $\Re(s) = -4$ and $\Re(s) = -8$, respectively.

Fig. 3 Considered input angular velocity waveforms



7.1 Robust Vibration Control Evaluation

Owing to the fabrication imperfections and ambient factors, parameters variations, and mechanical couplings are inevitable in a real gyroscope. To take this into account, the off-diagonal stiffness and damping constants k_{xy} , d_{xy} are assumed to be 5% of the corresponding x-axis nominal parameters k_{xx}^n , d_{xx}^n . Additionally, relatively large variations of $\pm 10\%$, from the nominal values, are considered for the diagonal stiffness and damping parameters k_{ii} , d_{ii} . To cover these parameters variation ranges, we assume d_{ii} = $d_{ii}^{n} (1 + 0.1\cos(20\pi t))$ and $k_{ii} = k_{ii}^{n} (1 + 0.1\cos(20\pi t))$ for $i \in \{x, y\}$. According to Consideration 1, the uncertain terms ΔK and ΔD include both off-diagonal and variations of the diagonal parameters. The input angular velocity is the waveform a₂ of Fig. 3. The mechanical-thermal noisy force is considered a zero mean random variable with the Gaussian distribution and power spectral density of $1.47 \times$ 10^{-26} N²s. The measurement noise of the sensing interface circuit is also modeled as a random signal with zero mean, normal distribution and power spectral density of 1.49 × $10^{-27} \text{ m}^2 \text{s}$ [7].

The tracking behavior of the controlled *x*-axis is shown in Fig. 4 for Cases I through IV. The regulated vibration of the *y*-axis is also depicted in Fig. 5. It is observed that after a settling time of 2 ms, the motion of the proof mass tracks the

reference trajectory. We note that the fast-tracking property of the controller substantially improves the performance of the angular velocity estimation algorithm. To illustrate the robustness of the control system in producing the desired tracking response in the presence of parametric uncertainty, the trajectories for $\Delta K = 0$, $\Delta D = 0$ and $\Omega_z = 0$ are also shown in Figs. 4 and 5. The root mean square (RMS) values of the difference between the two tracking responses are: $1.8 \times 10^{-4} \mu \text{m}$ for Case I, $1.4 \times 10^{-3} \mu \text{m}$ for Case II, $1.8 \times 10^{-3} \mu \text{m}$ for Case III and $1.3 \times 10^{-3} \mu \text{m}$ for Case IV. Additionally, under the resonance condition (the reference trajectory of Case III) over the time interval [0, 100]ms, Fig. 6 shows the statistical properties of the tracking error signals for various parameter variations. According to these results, the control system shows an excellent robustness in terms of continuity and small variations with respect to the changes in gyroscope parameters. In order to investigate robustness against the mechanical-thermal and measurement noises, we define the truncated \mathcal{L}_2 norms

$$g_{\tau} \triangleq \frac{\|\operatorname{col}(x, y) - \operatorname{col}(\bar{x}_{\tau}, \bar{y}_{\tau})\|_{\mathcal{L}_{2T}}}{\|\tau\|_{\mathcal{L}_{2T}}},$$

$$g_{\nu} \triangleq \frac{\|\operatorname{col}(x, y) - \operatorname{col}(\bar{x}_{\nu}, \bar{y}_{\nu})\|_{\mathcal{L}_{2T}}}{\|\nu\|_{\mathcal{L}_{2T}}},$$
(45)

where $\operatorname{col}(\bar{x}_{\tau}, \bar{y}_{\tau}) \in \mathbb{R}^2$ and $\operatorname{col}(\bar{x}_{\nu}, \bar{y}_{\nu}) \in \mathbb{R}^2$ are closed-loop vibration trajectories with $\tau \equiv 0$ and $\nu \equiv 0$, respectively. The norms g_{τ} and g_{ν} provide an energy

Table 2 Results of numerical solution of the LMIs (24a)-(24c)

Case	I	II	III	IV
γ $\lambda_{max}(P)$ $\lambda_{min}(P)$ $\max\{\Re \left(\lambda_i(A_0 + \sigma H C_0)\right)\}$ $\min\{\Re \left(\lambda_i(A_0 + \sigma H C_0)\right)\}$	7.0402×10^{7} 9.2867×10^{5} 1.7079×10^{-4} -12.1679 -15.6340	4.3939×10^{7} 5.4137×10^{5} 1.5075×10^{-4} -12.6665 -16.1804	2.9307×10^{7} 4.0681×10^{5} 1.3662×10^{-4} -12.2952 -16.5202	7.9853×10^{7} 1.1109×10^{6} 1.3790×10^{-4} -13.0396 -16.4480



Fig. 4 Tracking behavior of the controlled *x*-axis: with parametric uncertainty (solid lines), without parametric uncertainty (dashed-dot lines) and the reference signals (dashed lines)

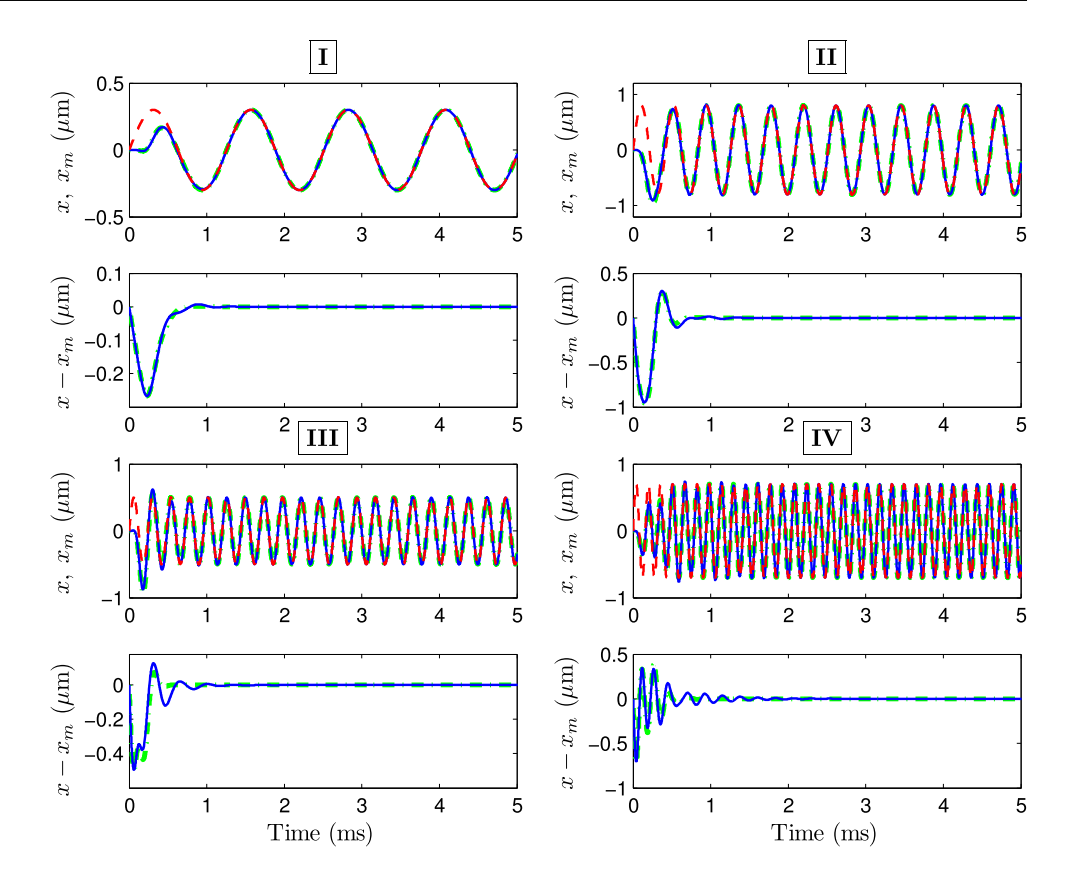


Fig. 5 Regulated vibration of the *y*-axis: with parametric uncertainty (solid lines) and without parametric uncertainty (dashed-dot lines)

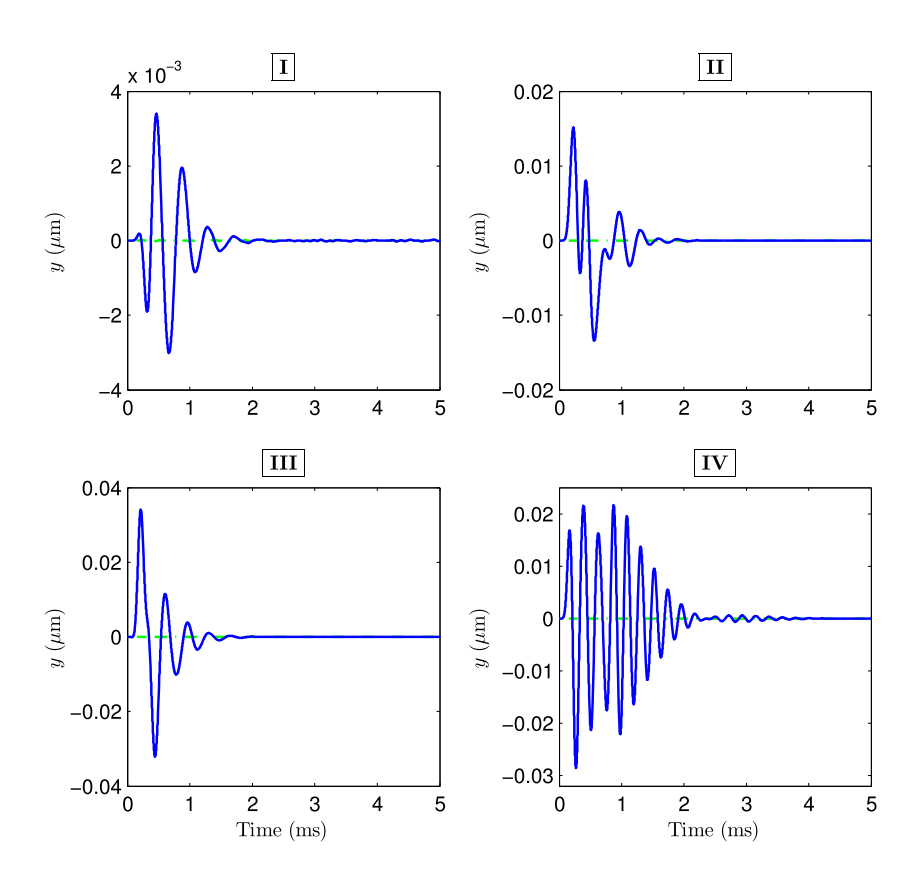
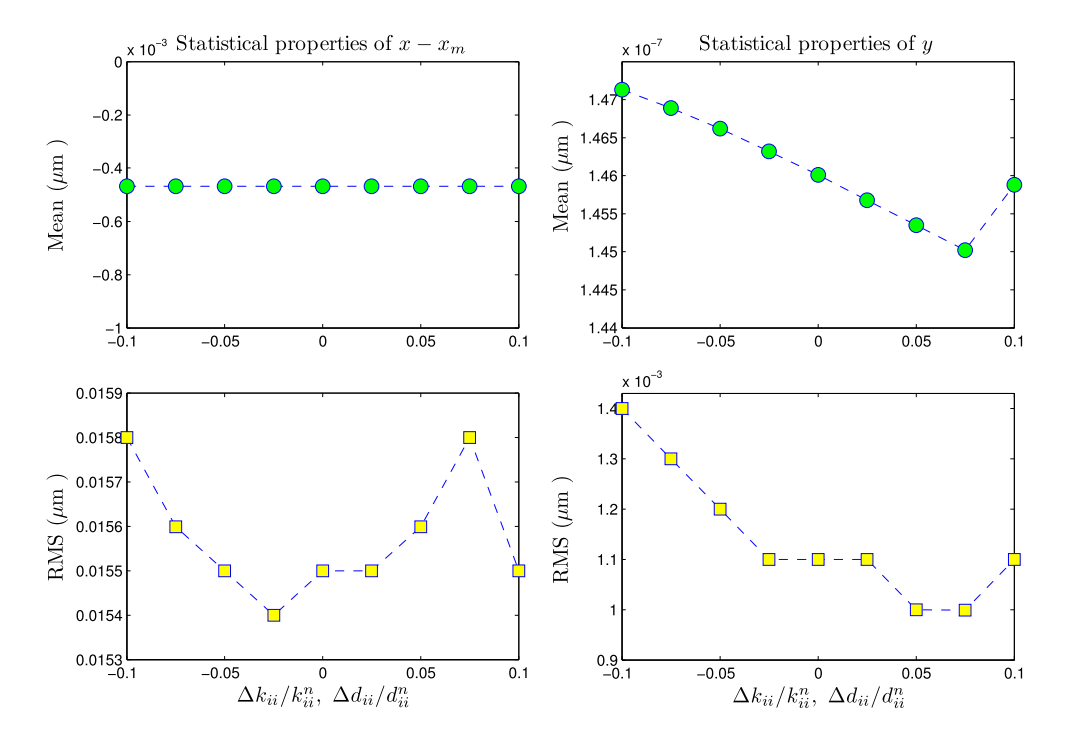




Fig. 6 Statistical properties of the tracking error signals of Case III versus variations of $\Delta d_{ii}/d_{ii}$, $\Delta k_{ii}/k_{ii}$



measure of the perturbation generated by the respective noises in the gyroscope vibration. Table 3 shows the numerical values of these norms for Cases I-IV over the closed-loop operation time [0, 100]ms. According to the values of g_{τ} and g_{ν} , the effect of the measurement noise on the gyroscope's vibration control is more significant than the mechanical-thermal noise. Therefore, the output feedback and the measurement noise are important issues that should be considered in a MEMS gyroscope controller. Interestingly, under the resonance condition, the effect of the mechanical-thermal noise on the gyroscope's vibration is minimized. This observation is in agreement with Remark 1.

The performance of the proposed vibration control method is compared with the conventional sliding mode [8] and the adaptive control techniques [7, 38]. For this purpose, the drive mode control of the gyroscope in the resonance condition is considered. The controllers are designed as follows:

Sliding mode controller [8]: Defining the sliding surface as $s \triangleq (\dot{x} - \dot{x}_m) + \alpha(x - x_m)$, $\alpha > 0$, the following control law is used for finite-time stabilization of s, with the assumption that there is no information about the bounds of the x-axis perturbation:

$$u_x = k_{11}^n (x - x_m) + (d_{11}^n - \alpha)\dot{x} + \alpha \dot{x}_m - \rho \operatorname{sign}(s),$$
 (46)

where $\rho > 0$ is the gain of the robust control term. In the simulation, using the reference values $q_0 = 10^{-6}$ m

and $w_0 = 1$ kHz, the parameters of the control law (46) are tuned as $\alpha = 5$ and $\rho = 500$.

 Adaptive controller [7, 38]: The velocity observerbased adaptive controller for the gyroscope is described by the following equations:

$$u = (\hat{D} - 2\hat{\Lambda}) \dot{q}_{m} + \hat{R}q_{m} + u_{0},$$

$$u_{0} = -\operatorname{diag}(\gamma_{1}, \gamma_{2}) (q_{v} - \dot{q}_{m}),$$

$$\dot{q}_{p} = q_{v} + \operatorname{diag}(l_{1}, l_{2})(q - q_{p}),$$

$$\dot{q}_{v} = -K_{m}q_{p},$$

$$\dot{\hat{D}} = \frac{1}{2}\gamma_{D} (u_{0}\dot{q}_{m}^{\top} + \dot{q}_{m}u_{0}^{\top}),$$

$$\dot{\hat{\Lambda}} = \frac{1}{2}\gamma_{\Lambda} (u_{0}\dot{q}_{m}^{\top} - \dot{q}_{m}u_{0}^{\top}),$$

$$\dot{\hat{R}} = \frac{1}{2}\gamma_{R} (u_{0}q_{m}^{\top} + q_{m}u_{0}^{\top}),$$

$$(47)$$

where $K_m \in \mathbb{R}^2$ determines the desired vibration frequencies. In order to compare the tracking performances of the adaptive controller and our proposed controller, the reference dynamics is selected as (29). According to the reference parameters $q_0 = 10^{-6}$ m and $w_0 = 26.201$ kHz, the parameters of the adaptive controller are tuned as $\gamma_1 = \gamma_2 = 1$, $\gamma_D = \gamma_R = 1/10$, $\gamma_{\Lambda} = 1/50$, and $l_1 = l_2 = 1$.

Comparative graphs of the tracking errors and the control efforts are shown in Fig. 7. The sliding mode controller shows the fastest transient response but, the steady-state tracking error of the proposed perturbation compensation-based controller is much smaller. The steady-state control signal for all methods has almost the same profile. However, both sliding mode and adaptive controllers show peaking in the transient part that could be harmful to the actuators.



Table 3 Numerical values of the norms g_{τ} and g_{ν} over the time interval [0, 100]ms

Case	I	II	III	IV
g_{τ} (m/N) g_{ν} (m/m)	1.7333×10^{-3} 0.2897	8.4947×10^{-4} 0.1827	6.7333×10^{-4} 0.2082	1.2225×10^{-3} 0.2137

Besides, the sliding mode control signal suffers from the chattering phenomenon. To compare the computational efficiency of the control methods, under the same simulation condition, we reach to the following simulation times: 10.8812 s for the proposed controller, 437.3082 s for the adaptive controller and 91.0043 s for the sliding mode controller. As a result, the proposed control method needs much less memory and computational effort, compared with the other two methods.

7.2 NESO Performance Evaluation

The NESO (11) is at the core of the perturbation compensation loop. To put the effectiveness of the proposed NESO in perspective, we compare its performance with the conventional linear high-gain ESO. Setting $x_1 = q$, $x_2 = \dot{q}$

and $x_3 = f(q, \dot{q}, t)$, the linear ESO for the gyroscope system (2) is given by

$$\dot{\hat{x}}_1 = \hat{x}_2 + \frac{\bar{H}_1}{\epsilon} (y - \hat{x}_1),
\dot{\hat{x}}_2 = -K_n \hat{x}_1 - D_n \hat{x}_2 + \hat{x}_3 + u + \frac{\bar{H}_2}{\epsilon^2} (y - \hat{x}_1),
\dot{\hat{x}}_3 = \frac{\bar{H}_3}{\epsilon^3} (y - \hat{x}_1),$$
(48)

where $\epsilon=10^{-3}$ is the high-gain parameter, $\bar{H}_1=\mathrm{diag}(3,3)$, $\bar{H}_2=\mathrm{diag}(3,3)$ and $\bar{H}_3=\mathrm{diag}(1,1)$. The convergence analysis of (48) can be found in [39]. To observe the peaking phenomenon, we consider the small off-track values $x(0)=0.03~\mu\mathrm{m},~y(0)=0.05~\mu\mathrm{m}$ for the proof mass. The perturbation $f(q,\dot{q},t)$ is considered with the same specifications of Section 7.1. Under the resonance vibration control, comparative graphs of the estimation errors of the proposed NESO (11) and the linear

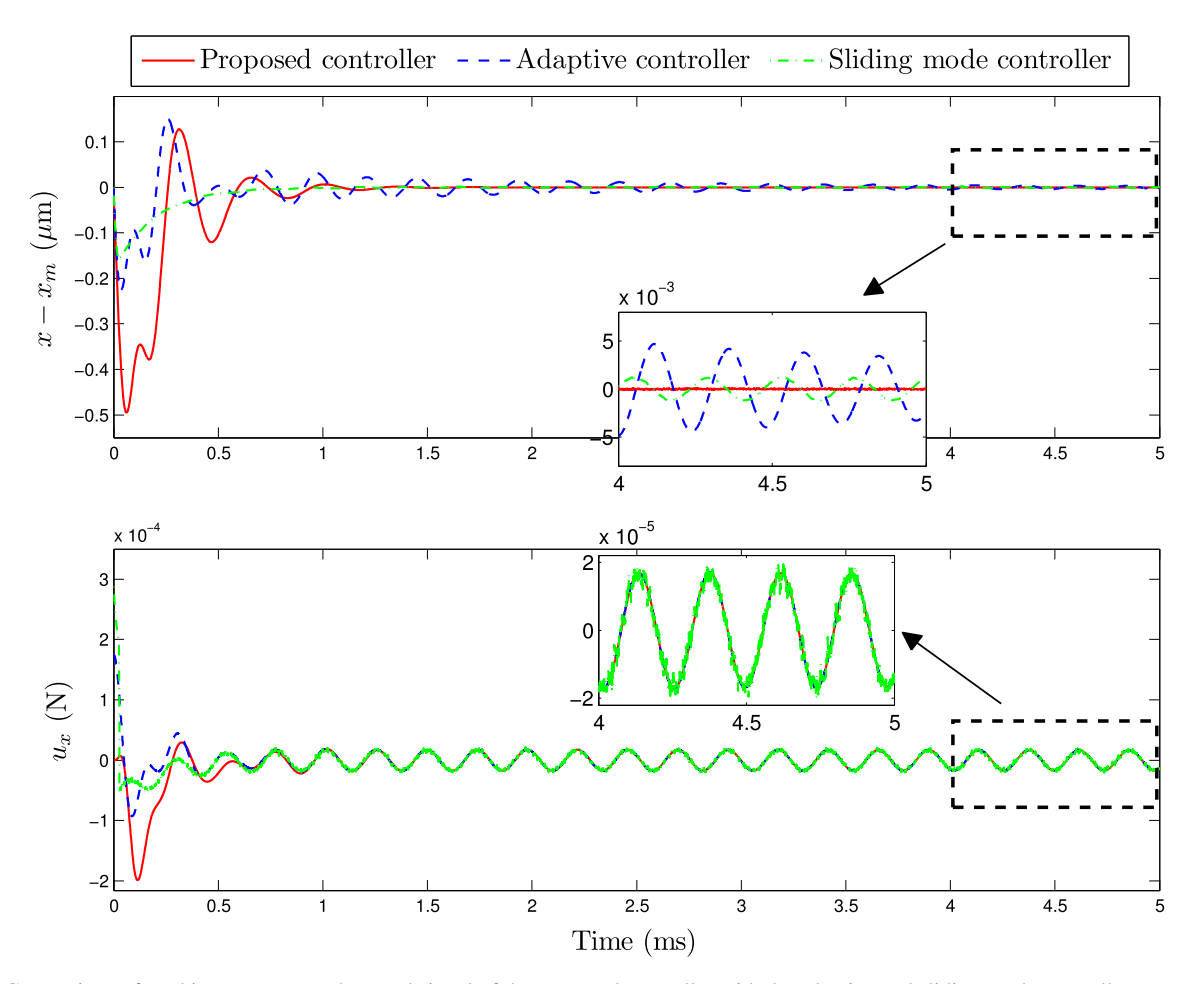


Fig. 7 Comparison of tracking response and control signal of the proposed controller with the adaptive and sliding mode controllers



Table 4 Statistical properties of estimation errors of the linear ESO and the proposed NESO

	Linear ESO Proposed NESO			
Error signal	Mean	RMS	Mean	RMS
$x - \hat{x} \; (\mu \text{m})$	5.9097×10^{-6}	6.1769×10^{-5}	1.1381×10^{-5}	3.8970×10^{-4}
$y - \hat{y} (\mu m)$	9.7580×10^{-6}	8.3489×10^{-5}	1.9287×10^{-5}	4.6800×10^{-4}
$\dot{x} - \hat{\dot{x}} \; (\mu \text{m/ms})$	-0.0022	0.0884	-4.1560×10^{-4}	0.0302
$\dot{y} - \hat{\dot{y}} \; (\mu \text{m/ms})$	-0.0037	0.1402	-7.0305×10^{-4}	0.0389
$f_x - \hat{f}_x \; (\mu N)$	0.0053	5.6023	-0.0022	0.5418
$f_y - \hat{f}_y (\mu N)$	0.0066	5.6249	-0.0038	0.5099

high-gain ESO (48) are shown in Fig. 8. The statistical properties of the estimation error signals are given in Table 4. In position estimation, the linear ESO has a much faster transient response, and the statistical properties of its error signals are better than our proposed ESO. Although, in the steady-state perspective, the estimation errors of the proposed NESO are smaller than the linear one. In velocity signal estimation, the proposed NESO outperforms the linear ESO in terms of the statistical properties of the error signals and the steady-state tracking error. In perturbation

estimation, the statistical properties of the error signals of the NESO are much better than the linear ESO. The amplitudes of the error signals of the latter are much larger. Besides, in both velocity and perturbation estimations, the linear ESO exhibits peaking during its transient phase. The linear high-gain observers amplify noises along the estimation of derivatives of the measured signal [30]. Thereby, using the internal model of the perturbation (8) and (9) along with the nonlinear gain (12) offers robustness against the measurement noise. Overall, the results validate

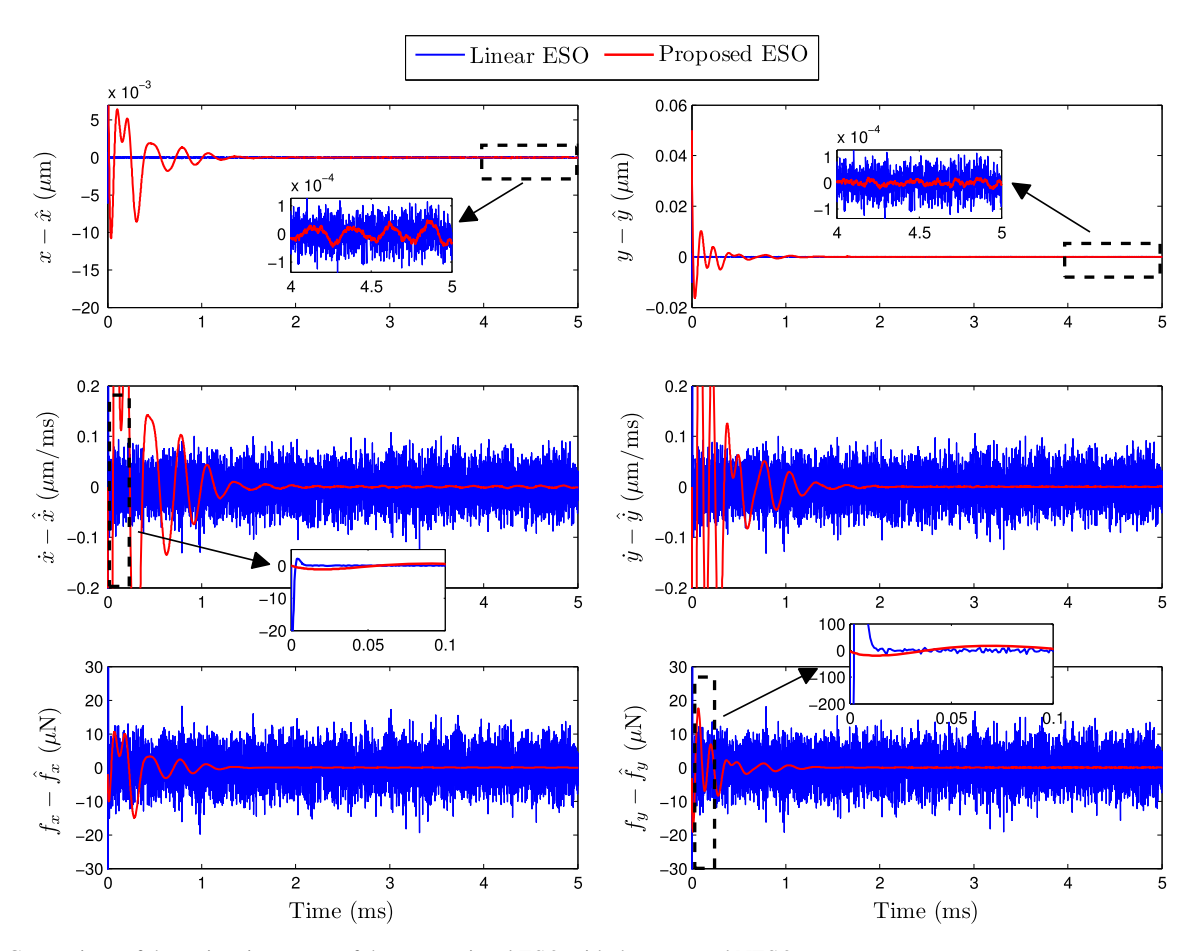


Fig. 8 Comparison of the estimation errors of the conventional ESO with the proposed NESO

the effectiveness of the proposed NESO in perturbation estimation and, in turn, providing a framework for angular velocity estimation.

7.3 Angular Velocity Estimation

To obtain the estimated perturbation for angular velocity estimation, in view of Remark 2, we propose the following least squares optimization:

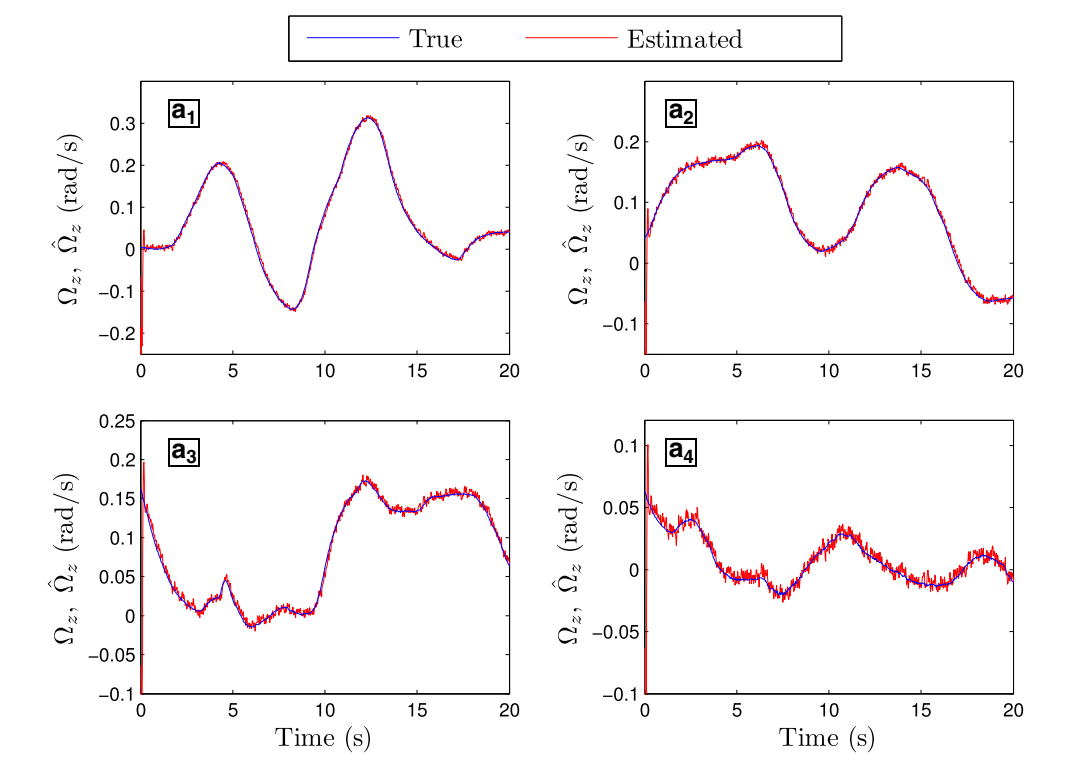
$$f_y^{est} \triangleq \arg\min_{f_y} \frac{(f_y - \hat{f}_y)^2}{\theta_1^2} + \frac{(f_y + u_y)^2}{\theta_2^2}.$$
 (49)

Therefore,

$$f_y^{est} = \frac{\theta_2^2 \hat{f}_y - \theta_1^2 u_y}{\theta_1^2 + \theta_2^2}.$$

In the formulation (49), θ_1^2 and θ_2^2 are variances of the estimations errors associated with \hat{f}_y and $-u_y$, respectively. Through a comparative simulation for a given perturbation f_y , we obtain $\theta_1 = 0.4695$ and $\theta_2 = 0.6171$. The operator Q of the estimator (7) is designed as the cascade of two operators Q_1 and Q_2 ;

Fig. 9 Estimation of the input angular velocity waveforms a_1 , a_2 , a_3 and a_4



1. The first operator is a fifth-order, type I Chebyshev lowpass filter with the cutoff frequency of 700 rad/s. The filter in the Laplace domain is given by

$$Q_1(s) = \frac{\frac{0.0688}{w_0^5}}{s^5 + \frac{1.2208}{w_0}s^4 + \frac{1.3576}{w_0^2}s^3 + \frac{0.8222}{w_0^3}s^2 + \frac{0.3447}{w_0^4}s + \frac{0.0688}{w_0^5}}$$

2. In order to remove the undesired fluctuations and improve the statistical properties of the estimation error, the second operator is designed as the following moving average operator:

$$Q_2 \colon \chi(t) \to \frac{1}{T_{ave}} \int_{t-T_{ave}}^{t} \chi(t') dt',$$

where $\chi(.)$ is the operand signal and $T_{ave} > 0$ is the averaging interval size. In the Laplace domain, this operator is described by the transfer function $Q_2(s) = (1 - \exp(-T_{ave}s)) / T_{ave}s$ which, like Q_1 , has low-pass filtering property.

In the zero rate condition, the bias term of (7) is identified as $\Omega_0 = -0.06359$ rad/s. Estimation of the considered angular velocity waveforms, under the working frequency of 50Hz, is shown in Fig. 9 and the statistical properties of the corresponding estimation error signals are given in Table 5. These results, confirm the fast adaptation property of the proposed estimator in tracking time-varying angular velocities. Besides, the estimator shows a good sensitivity



Table 5 Statistical properties of the angular velocity estimation error $\Omega_z - \hat{\Omega}_z$

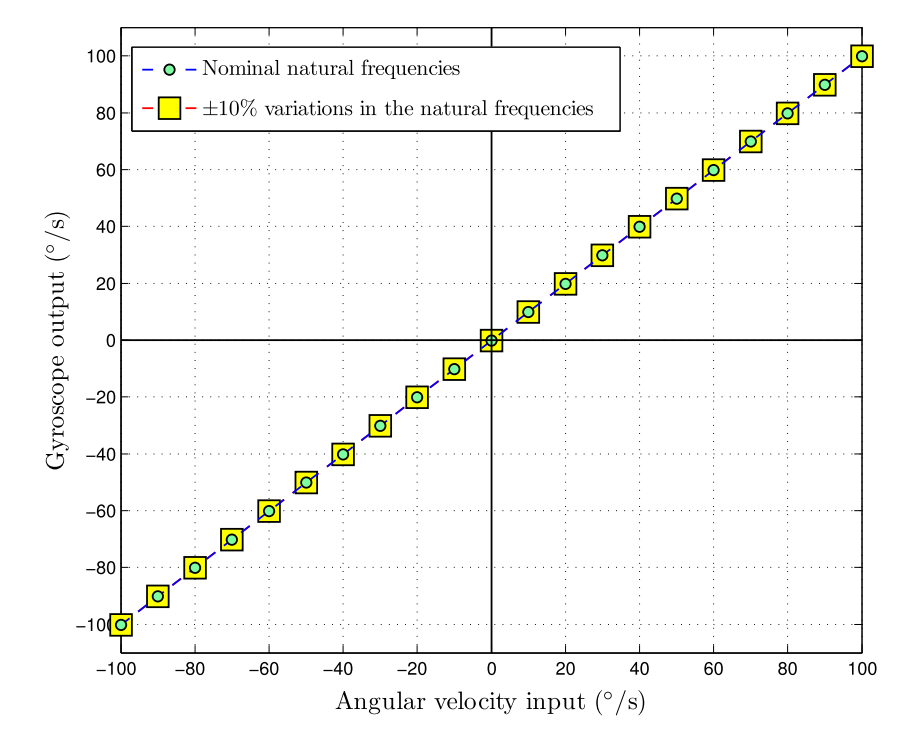
Angular velocity waveform	Mean value of the estimation error (rad/s)	RMS value of the estimation error (rad/s)
a_1	1.1318×10^{-4}	0.0174
a_2	-1.3812×10^{-4}	0.0182
a_3	2.5911×10^{-4}	0.0224
a ₄	-1.1503×10^{-4}	0.0187

in detecting and identifying the angular velocities of a typical navigational application. In the conventional mode of operation, the scale factor of the sensor is very sensitive to parameter variations, especially in the natural frequencies [4]. In this regard, to illustrate robust angular velocity estimation of the proposed closed-loop system, Fig. 10 shows the steady-state mean values of the gyroscope outputs for the input range $[-100, 100](^{\circ}/s)$. We consider two cases: (i) no variation in the natural frequencies, (ii) 10% variation in the natural frequencies. The input-output curves of both cases almost coincide with each other. The results indicate the robustness of the estimator against parameter variations.

7.4 Comments for Implementation

The computational algorithm of the proposed closed-loop system, in essence, demands the numerical solution of a set of ordinary differential equations. Therefore, real-time implementation of the controller on a manufactured MEMS gyroscope can be performed by common programmable digital control platforms. For example, the designed control method can be executed on a micro DSP/FPGA which commonly produces the control signals as PWM outputs. The parameters and gains of the control system require offline computations which, in turn, simplify the real-time execution of the whole control system. Discretization of the involved differential equation can be performed by the Euler's forward method. The output feedback controller (38) can be designed by the standard linear control methods such as LQR or eigenvalue assignment to obtain the desired transient performance. The efficient solution of the LMIs (24a)-(24c), which are standard convex programming problems, is acquirable through software packs like CVX or MATLAB LMI toolbox. For the digital implementation of the angular velocity estimator (7), the Q operator can be discretized using Euler's method $s \approx (z - 1)/\Delta t$ where Δt is the sampling time, and z is the z-transform variable equivalent to the forward shift operator. The digital control section is connectable to the actuation/sensing circuits of the MEMS gyroscope by digital-to-analog and analog-to-digital converters.

Fig. 10 The angular velocity input versus the gyroscope output, in the range [-100, 100](°/s), for the proposed closed-loop mode of operation





8 Conclusions and Future Works

In this paper, a new closed-loop operation strategy was developed for single-axis MEMS gyroscopes based on the perturbation compensation method. First, the angular velocity estimation was performed in the force-balancing framework. Next, a control system was designed to regulate the gyroscope vibration and drive its energy to a suitable level. The simulation results confirmed robust and fast-tracking response of the control system. The performance of the angular velocity estimator was tested by applying the experimental data of a real-time gyroscope application in a vehicle INS/GPS system. It is observed that the estimator correctly identifies the profile of time-varying input angular velocities. The proposed closed-loop configuration can be applied to the existing gyroscopes to improve their performance specifications like bandwidth and sensitivity.

Further investigation on practical aspects of the proposed closed-loop operation mode, including sensing/actuation circuitry and integration with the control execution platform, outlines the future direction of this research work. Moreover, the design of improved perturbation estimators for other classes of MEMS sensors, such as torsional and angle measuring gyroscopes, will be pursued by the authors in the future works. The focus will be on the output feedback control through noisy and imperfect measurements in the MEMS devices that utilize capacitive detection. Since nanoscale sensors in the field of inertial measurements are expected to be developed in a close future, the modeling, identification and control aspects of this technology would be a part of future research.

References

- Doostdar, P., Keighobadi, J.: Design and implementation of SMO for a nonlinear MIMO AHRS. Mech. Syst. Signal Process. 32, 94–115 (2012)
- Zhanshe, G., Fucheng, C., Boyu, L., Le, C., Chao, L., Ke, S.: Research development of silicon MEMS gyroscopes: a review. Microsystem Technol. 21(10), 2053–2066 (2015)
- Yazdi, N., Ayazi, F., Najafi, K.: Micromachined inertial sensors. Proc. IEEE 86(8), 1640–1658 (1998)
- Acar, C., Shkel, A.: MEMS vibratory gyroscopes: structural approaches to improve robustness. MEMS Reference Shelf. Springer, Boston (2009)
- Park, S., Horowitz, R.: Adaptive control for the conventional mode of operation of MEMS gyroscopes. J. Microelectromech. Syst. 12(1), 101–108 (2003)
- Shkel, A., Howe, R.T., Horowitz, R.: Modeling and Simulation of Micromachined Gyroscopes in The Presence of Imperfections. In: International Conference on Modeling and Simulation of Microsystems, pp. 605–608 (1999)
- Park, S., Horowitz, R.: Adaptive control for z-axis MEMS gyroscopes. In: Proceedings of the 2001 American Control Conference, pp. 1223–1228, Arlington (2001)

- Batur, C., Sreeramreddy, T., Khasawneh, Q.: Sliding mode control of a simulated MEMS gyroscope. ISA Trans. 45(1), 99–108 (2006)
- Fei, J., Batur, C.: A novel adaptive sliding mode control with application to MEMS gyroscope. ISA Trans. 48(1), 73–78 (2009)
- Fei, J., Yan, W.: Adaptive control of MEMS gyroscope using global fast terminal sliding mode control and fuzzy-neuralnetwork. Nonlinear Dyn. 78(1), 103–116 (2014)
- Hosseini-Pishrobat, M., Keighobadi, J.: Force-balancing model predictive control of MEMS vibratory gyroscope sensor. Proc Inst. Mech. Eng. Part C: J. Mech. Eng. Sci. 230(17), 3055–3065 (2016)
- Zheng, Q., Dong, L., Gao, Z.: Control and Rotation Rate Estimation of Vibrational MEMS Gyroscopes. In: 2007 IEEE International Conference on Control Applications, pp. 118–123 (2007)
- Zheng, Q., Lee, D.H., Dong, L., Gao, Z.: Active Disturbance Rejection Control for MEMS Gyroscopes. IEEE Trans. Control Syst. Technol. 17(6), 1432–1438 (2009)
- Kwon, S., Chung, W.K.: Perturbation compensator based robust tracking control and state estimation of mechanical systems, Lecture Notes in Control and Information Sciences, vol. 307 Springer Science & Business Media (2004)
- Huang, Y., Xue, W.: Active disturbance rejection control: Methodology and theoretical analysis. ISA Trans. 53(4), 963–976 (2014)
- Madoński, R., Herman, P.: Survey on methods of increasing the efficiency of extended state disturbance observers. ISA Trans. 56, 18–27 (2015)
- Rodriguez-Fortun, J.M., Orus, J., Alfonso, J., Gimeno, F.B., Castellanos, J.A.: Flatness-based active vibration control for piezoelectric actuators. IEEE/ASME Trans. Mechatronics 18(1), 221–229 (2013)
- Wei, J.J., Qiu, Z.C., Han, J.D., Wang, Y.C.: Experimental Comparison Research on Active Vibration Control for Flexible Piezoelectric Manipulator Using Fuzzy Controller. J. Intell. Robot. Syst. 59(1), 31–56 (2010)
- He, W., Nie, S., Meng, T., Liu, Y.J.: Modeling and vibration control for a moving beam with application in a drilling riser. IEEE Trans. Control Syst. Technol. 25(3), 1036–1043 (2017)
- Zhao, Z., Liu, Y., Guo, F., Fu, Y.: Vibration control and boundary tension constraint of an axially moving string system. Nonlinear Dyn. 89(4), 2431–2440 (2017)
- He, W., He, X., Sun, C.: Vibration Control of an Industrial Moving Strip in the Presence of Input Deadzone. IEEE Trans. Ind. Electron. 64(6), 4680–4689 (2017)
- Zhao, Z., Liu, Y., He, W., Luo, F.: Adaptive boundary control of an axially moving belt system with high acceleration/deceleration. IET Control Theory Appl. 10(11), 1299–1306 (2016)
- He, W., Meng, T., Huang, D., Li, X.: Adaptive Boundary Iterative Learning Control for an Euler-Bernoulli Beam System With Input Constraint. IEEE Trans. Neural Netw. Learn. Syst. PP(99), 1–8 (2017)
- He, W., Ouyang, Y., Hong, J.: Vibration control of a flexible robotic manipulator in the presence of input deadzone. IEEE Trans. Ind. Inform. 13(1), 48–59 (2017)
- He, W., Meng, T.: Adaptive Control of a Flexible String System With Input Hysteresis. IEEE Transactions on Control Systems Technology, PP(99), 1–8 (2017)
- Zhao, Z., Liu, Y., Luo, F.: Output feedback boundary control of an axially moving system with input saturation constraint. ISA Trans. 68, 22–32 (2017)
- Xin, M., Fei, J.: Adaptive vibration control for MEMS vibratory gyroscope using backstepping sliding mode control. J. Vibr. Control 21(4), 808–817 (2015)



- He, W., Yin, Z., Sun, C.: Adaptive neural network control of a marine vessel with constraints using the asymmetric barrier lyapunov function. IEEE Trans. Cybern. 47(7), 1641–1651 (2017)
- Isidori, A., Marconi, L., Serrani, A.: Robust Autonomous Guidance: An Internal Model Approach. Advances in Industrial Control Springer London (2003)
- Prasov, A.A., Khalil, H.K.: A nonlinear high-gain observer for systems with measurement noise in a feedback control framework. IEEE Trans. Autom. Control 58(3), 569–580 (2013)
- Chen, Z., Huang, J.: Robust Output Regulation: A Framework.
 In: Stabilization and Regulation of Nonlinear Systems, Advanced Textbooks in Control and Signal Processing, chap. 7, pp. 197–237.
 Springer International Publishing (2015)
- 32. Gabrielson, T.B.: Mechanical-thermal noise in micromachined acoustic and vibration sensors. IEEE Trans. Electron Devices 40(5), 903–908 (1993)
- Boyd, S., Ghaoui, L.E., Feron, E., Balakrishnan, V.: Linear Matrix Inequalities in System and Control Theory. Studies in Applied Mathematics Society for Industrial and Applied Mathematics (1994)
- Khalil, H.K. Nonlinear Systems, 3rd edn. Pearson Education, Prentice Hall (2002)
- Musavi, N., Keighobadi, J.: Adaptive fuzzy neuro-observer applied to low cost INS/GPS. Appl. Soft Comput. 29, 82–94 (2015)
- Grant, M., Boyd, S.: CVX: Matlab Software for Disciplined Convex Programming, version 2.1. http://cvxr.com/cvx (2014)

- Grant, M., Boyd, S.: Graph implementations for nonsmooth convex programs. In: Blondel, V., Boyd, S., Kimura, H. (eds.) Recent Advances in Learning and Control, Lecture Notes in Control and Information Sciences, pp. 95–110. Springer-Verlag Limited (2008)
- Park, S., Horowitz, R.: Discrete time adaptive control for a MEMS gyroscope. Int. J. Adapt. Control Signal Process. 19(2003), 485– 503 (2005)
- Guo, B.Z., liang Zhao, Z.: On the convergence of an extended state observer for nonlinear systems with uncertainty. Syst. Control Lett. 60(6), 420–430 (2011)

Mehran Hosseini-Pishrobat received his M.S. degree in mechanical engineering from University of Tabriz, Iran, in 2016. His research interests include control of MEMS/NEMS, nonlinear control, and disturbance estimation-based control.

Jafar Keighobadi received his Ph.D. degree in mechanical engineering and control systems from Amirkabir University of Technology in Tehran, Iran in 2008. He joined the Faculty of Mechanical Engineering, University of Tabriz, as an assistant professor in 2008. Dr. Keighobadi's research interests include estimation and control of stochastic systems and the applications in MEMS, robotic and navigation systems.

